

Raman spectroscopy as a versatile tool for studying the properties of graphene

Andrea C. Ferrari^{1*} and Denis M. Basko²

Raman spectroscopy is an integral part of graphene research. It is used to determine the number and orientation of layers, the quality and types of edge, and the effects of perturbations, such as electric and magnetic fields, strain, doping, disorder and functional groups. This, in turn, provides insight into all sp^2 -bonded carbon allotropes, because graphene is their fundamental building block. Here we review the state of the art, future directions and open questions in Raman spectroscopy of graphene. We describe essential physical processes whose importance has only recently been recognized, such as the various types of resonance at play, and the role of quantum interference. We update all basic concepts and notations, and propose a terminology that is able to describe any result in literature. We finally highlight the potential of Raman spectroscopy for layered materials other than graphene.

Graphene is the two-dimensional building block for sp^2 carbon allotropes of every other dimensionality. It can be stacked into three-dimensional graphite, rolled into one-dimensional nanotubes, or wrapped into zero-dimensional fullerenes. It is at the centre of an ever-expanding research area^{1–5}. Near-ballistic transport and high mobility make it an ideal material for nanoelectronics, especially for high-frequency applications⁶. Furthermore, its optical and mechanical properties are ideal for micro- and nanomechanical systems, thin-film transistors, transparent and conductive composites and electrodes, flexible and printable (opto)electronics, and photonics^{2–4,7,8}.

An ideal characterization tool should be fast and non-destructive, offer high resolution, give structural and electronic information, and be applicable at both laboratory and mass-production scales. Raman spectroscopy^{9,10} fulfils all these requirements. The Raman spectrum of graphite was first recorded more than 40 years ago¹¹ and, by the time the Raman spectrum of graphene was first measured in 2006¹², Raman spectroscopy had become one of the most popular techniques for the characterization of disordered and amorphous carbons, fullerenes, nanotubes, diamonds, carbon chains and polyconjugated molecules¹³. Raman techniques are particularly useful for graphene¹⁴ because the absence of a bandgap makes all wavelengths of incident radiation resonant, thus the Raman spectrum contains information about both atomic structure and electronic properties. Resonance could also be reached by ultraviolet excitation^{15,16}, either with the M-point Van Hove singularity or in the case of bandgap opening, such as in fluorinated graphene.

The number of graphene layers (N) in a sample can be determined by elastic light scattering (Rayleigh) spectroscopy^{17,18}, but this approach only works for exfoliated samples on optimized substrates and does not provide other structural or electronic information. Raman spectroscopy, on the other hand, works for all graphene samples^{12,14}. Moreover, it is able to identify unwanted by-products, structural damage, functional groups and chemical modifications introduced during the preparation, processing or placement of graphene⁵. As a result, a Raman spectrum is invaluable for quality control, and for comparing samples used by different research groups.

The toll for the simplicity of Raman measurements is paid when it comes to data interpretation. The spectra of all carbon-based materials show only a few prominent features, regardless of the final structure¹³. However, the shapes, intensities and positions of these peaks give a considerable amount of information, often comparable to that obtained by competing techniques that are more complicated and destructive¹³. For example, Raman spectroscopy can distinguish between a hard amorphous carbon, a metallic nanotube or a doped graphene sample¹⁴.

In the past six years, there has been a significant step forward in the understanding of Raman spectroscopy in graphene, fuelled by new results on doping^{19–27}, edges^{28–33}, strain and stress^{34–40}, disorder^{14,33,41–43}, oxidation⁴⁴, hydrogenation⁴⁵, chemical functionalization⁴⁶, electrical mobility^{47,48}, thermal conductivity^{49,50}, electron–phonon^{41,50–55} and electron–electron^{51,53,54,56,57} interactions, magnetic field^{58–67} and interlayer coupling^{68–72}. As a result, the understanding of the basic Raman processes has changed. Raman scattering on phonons is to a large extent determined by electrons: how they move, interfere and scatter. Thus, any variation of electronic properties due to defects, edges, doping or magnetic fields affects positions, widths and intensities of the Raman peaks, enabling one to probe electrons via phonons. Quantum interference effects^{20,52,73} play a key role, and they can also be investigated by this technique.

Here we review these new developments, and incorporate them into a general framework for Raman spectroscopy in graphene based on a unified and self-consistent terminology. We introduce the basic physics of Raman spectroscopy in graphene, and discuss the effects of edges, layers, defects and disorder, and perturbations. We outline the history of the field, interference^{74,75} and surface-enhanced⁷⁶ Raman scattering in the Supplementary Information (Sections S4, S2 and S3, respectively), along with the effects of polarization (Supplementary Section S5), electric fields and doping (Supplementary Section S6), magnetic field (Supplementary Section S7), uniaxial and biaxial strain (Supplementary Section S8), temperature (Supplementary Section S9), isotopes (Supplementary Section S10) and other examples (Supplementary Section S11). The key difference between our framework and those published previously^{77–79} is

¹Cambridge Graphene Centre, Cambridge University, 9 JJ Thomson Avenue, Cambridge CB3 0FA, UK, ²Université Grenoble 1 and CNRS, LPMMC UMR 5493, Grenoble, France. *e-mail: acf26@eng.cam.ac.uk

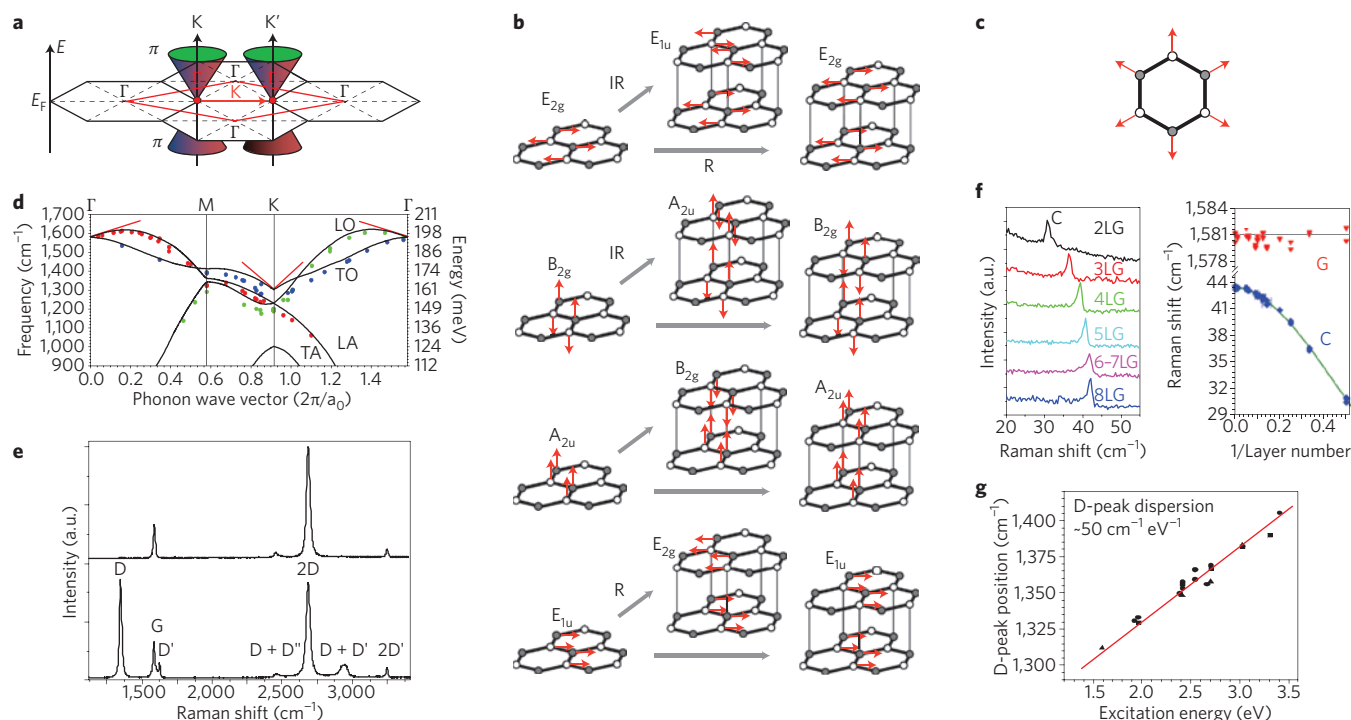


Figure 1 | Electrons, phonons and Raman spectrum of graphene. **a**, Electronic Brillouin zones of graphene (black hexagons), the first-phonon Brillouin zone (red rhombus) and schematic of electronic dispersion (Dirac cones). The phonon wave vectors connecting electronic states in different valleys are labelled in red. **b**, Γ -point phonon-displacement pattern for graphene and graphite. Empty and filled circles represent inequivalent carbon atoms. Red arrows show atom displacements. Grey arrows show how each phonon mode in graphene gives rise to two phonon modes of graphite. Their labelling shows Raman-active (R), infrared-active (IR) and inactive (unlabelled) modes. **c**, Atom displacements (red arrows) for the A_{1g} mode at K . **d**, The black curves represent the dispersion of in-plane phonon modes in graphene in the energy and frequency range relevant for Raman scattering. The red lines represent Kohn anomalies⁸⁰. The symbols are data taken from refs 54,84. **e**, Raman spectra of pristine (top) and defected (bottom) graphene. The main peaks are labelled. **f**, C peak as a function of number of layers (left). Fitted C- and G-peak position as a function of inverse number of layers (right). The line passing through the C-peak data is from equation (1). Flakes with N layers are indicated by NLG. Thus, for example, 2LG is BLG (bilayer graphene), and 8LG is 8-layer graphene. **g**, D-peak position as a function of excitation energy, data from ref. 87.

that we start from the general picture of the Raman process, and show how the numerous observed effects naturally arise from it. This approach creates a unified view of Raman scattering, thereby enabling the observed effects to be better understood and, hopefully, to anticipate new ones.

The Raman spectrum of graphene

To understand the state of the art in Raman spectroscopy of graphene it is important to know the historical development of the main ideas, nomenclature and peak assignments starting from graphite. We give a detailed overview in Supplementary Section S4, where we also introduce some background concepts, such as Kohn anomalies⁸⁰. Here we summarize the nomenclature and current understanding of the main peaks.

Throughout this Review we will use the notation I for peak height, A for peak area, Pos for peak position, FWHM for the full-width at half-maximum and $Disp$ for peak dispersion (that is, the rate of shift in peak position with changing excitation energy). So, for example, $I(G)$ is the height of the G peak, $A(G)$ its area, $FWHM(G)$ the full-width at half-maximum, $Pos(G)$ its position and $Disp(G)$ its dispersion.

The phonon dispersions of single-layer graphene (SLG) comprise three acoustic (A) and three optical (O) branches. The modes with out-of-plane (Z) motion are considerably softer than the in-plane longitudinal (L) and transverse (T) ones. Figure 1a plots the electronic Brillouin zone of graphene, the first-phonon Brillouin zone and shows a schematic of the electronic dispersion

(Dirac cones). Graphene has two atoms per unit cell, thus six normal modes (two being doubly degenerate) at the Brillouin zone centre Γ (ref. 81): $A_{2u} + B_{2g} + E_{1u} + E_{2g}$ (Fig. 1b) (ref. 82). There is one degenerate in-plane optical mode, E_{2g} , and one out-of-plane optical mode B_{2g} (ref. 81). The E_{2g} phonons are Raman active, whereas the B_{2g} phonon is neither Raman nor infrared active⁸¹. Graphite has four atoms per unit cell. Indeed, only half the carbons have fourth neighbours that lie directly above or below in adjacent layers. Therefore, the two atoms of the unit cell in each layer are now inequivalent. This doubles the number of optical modes, and is responsible for the infrared activity of graphite⁸¹. All the optical modes become Davydov-doublers: The E_{2g} phonon generates an infrared-active E_{1u} phonon and a Raman-active E_{2g} phonon, the B_{2g} phonon goes into an infrared-active A_{2u} phonon and an inactive B_{2g} phonon. The antisymmetric combinations of the acoustic modes are the optically inactive B_{2g} phonons and the Raman active E_{2g} modes. The symmetric combinations of the acoustic modes remain A_{2u} and E_{1u} (ref. 81). Thus, for graphite^{81–83} $\Gamma = 2(A_{2u} + B_{2g} + E_{1u} + E_{2g})$ (Fig. 1b). There are now two Raman active E_{2g} modes, each doubly degenerate.

The Raman spectrum of SLG consists of distinct bands¹² (Fig. 1e). Figure 1d plots the optical phonon dispersions of SLG, relevant for the interpretation of the Raman spectra^{54,80,84}. The G peak corresponds to the high-frequency E_{2g} phonon at Γ . The D peak is due to the breathing modes of six-atom rings (Fig. 1c) and requires a defect for its activation^{11,15,85}. It comes from TO phonons around the Brillouin zone corner K (refs 11,15), it is active by

double resonance^{85,86}, and is strongly dispersive with excitation energy⁸⁷ (Fig. 1g), due to a Kohn anomaly at **K** (ref. 80). Double resonance can also happen as an intravalley process, that is, connecting two points belonging to the same cone around **K** (or **K'**). This gives the so-called D' peak. The 2D peak is the D-peak overtone, and the 2D' peak is the D' overtone. Because the 2D and 2D' peaks originate from a process where momentum conservation is satisfied by two phonons with opposite wave vectors, no defects are required for their activation, and are thus always present^{12,88}.

The band at $\sim 2,450\text{ cm}^{-1}$ in Fig. 1e was first reported in graphite by Nemanich and Solin⁸⁹. Its interpretation was subject to debate, as discussed in Supplementary Section S4. It is assigned a combination of a D phonon and a phonon belonging to the LA branch, seen at $\sim 1,100\text{ cm}^{-1}$ in defected samples when measured with visible light, and called D'' peak^{55,90–93}, it is indicated as D + D'' in Fig. 1e.

The Raman spectrum of graphite and multilayer graphene consists of two fundamentally different sets of peaks. Those, such as D, G, 2D and so on, present also in SLG, and due to in-plane vibrations^{12–14}, and others, such as the shear (C) modes⁶⁸ and the layer-breathing modes (LBMs)^{69–71}, due to relative motions of the planes themselves, either perpendicular or parallel to their normal. The low-frequency E_{2g} mode in graphite was first measured by Nemanich *et al.* in 1975⁹⁴ at $\sim 42\text{ cm}^{-1}$. We called this mode C, because it is sensitive to the interlayer coupling⁶⁸ (Fig. 1f). The absence of the C peak would, in principle, be the most direct evidence of SLG. However, it is not warranted to use the absence of a peak as a characterization tool, because one can never be sure why something is absent. On the other hand, this mode scales with the number of layers, going to $\sim 31\text{ cm}^{-1}$ for bilayer graphene⁶⁸ (BLG) (Fig. 1f). The C-peak frequency is below the notch and edge filter cut-off of many spectrometers, particularly those used for production-line monitoring. This problem was overcome recently by combining a BraggGrate filter with a single monochromator⁶⁸ and, for the first time, Pos(C) was measured for an arbitrary number of graphene layers⁶⁸. This method allows the detection of similar modes in any other layered material^{68,95}. For Bernal stacked samples, Pos(C) varies with N as⁶⁸:

$$\text{Pos(C)}_N = \sqrt{\frac{2\alpha}{\mu}} \sqrt{1 + \cos\left(\frac{\pi}{N}\right)} \quad (1)$$

where $\alpha = 12.8 \times 10^{18}\text{ N m}^{-3}$ is the interlayer coupling, and $\mu = 7.6 \times 10^{-27}\text{ kg \AA}^{-2}$ is the graphene mass per unit area⁶⁸. Layer-breathing modes can also be observed in the Raman spectra of FLGs, through their resonant overtones and combination modes in the range $80\text{--}300\text{ cm}^{-1}$ (refs 69–71). Note that, although being an in-plane mode, the 2D peak is sensitive to N because the resonant Raman mechanism that gives rise to it is closely linked to the details of the electronic band structure^{12,14}, the latter changing with N , and the layers relative orientation⁹⁶. On the other hand, the C peak and LBMs are a direct probe of N (refs 55,68–72), as the vibrations themselves are out of plane, thus directly sensitive to N . Because the fundamental LBM in bulk graphite is a silent B_{1g} mode at $\sim 128\text{ cm}^{-1}$, the observation of the first-order LBM is a challenge.

Raman spectroscopy can also probe the scattering of photons by electronic excitations. In pristine graphene, these have a continuous structureless spectrum⁹⁷, not leading to any sharp feature. However, it was realized that in a strong magnetic field, B , when the electronic spectrum consists of discrete Landau levels, the electronic inter-Landau-level excitations give rise to sharp B -dependent peaks in the Raman spectrum^{60–62,98,99}.

Raman processes in graphene

The understanding of Raman processes in graphite and related

materials has challenged researchers for decades. The reason is the richness of phenomena combined with the wealth of experimental information that must be consistently arranged to solve the jigsaw. An introduction to Raman scattering is presented in Supplementary Section S1, whereas surface-enhanced and interference-enhanced Raman spectroscopy in graphene are discussed in Supplementary Sections S2 and S3.

In graphene, graphite and nanotubes, Raman processes involving up to six phonons can be easily measured^{90–92,100,101}. However, most literature reports spectra up to $\sim 3,300\text{ cm}^{-1}$. This restricts our attention to one- and two-phonon peaks. We can also distinguish between spectra measured on pristine samples (that is, ideally defect-free, undoped, unstrained and so on) and those measured on samples subject to external perturbations (such as electric and magnetic fields, strains and so on) or those with defects. We will cover external perturbations below, as well as in Supplementary Sections S6–S9. Defect-activated peaks will be discussed now together with those not requiring defects for their activation.

In general, Raman scattering can be described by perturbation theory¹⁰². An n -phonon process involves $n + 1$ intermediate states, and is described by an $(n + 2)$ -order matrix element, as given by equation (S-3) in the Supplementary Information. Figure 2 plots the possible elementary steps of the Raman processes contributing to each peak of graphene. According to the number of factors in the denominator of equation (S3) that vanish, the processes can be classified as double resonant (Fig. 2b–g,j,k) or triple resonant (Fig. 2h,i,l). Higher orders are also possible in multiphonon processes. Note that this classification is useful, but approximate (valid when the electron–hole asymmetry and the difference in energies of the two phonons are neglected). The process in Fig. 2a is not resonant.

One-phonon modes in defect-free samples can be Raman active only if their symmetry is correct and their wave vector is zero (that is, they obey the fundamental Raman selection rule, see Supplementary Section S1). In graphene, only the C and G peaks satisfy these requirements. The energies of the intermediate states are given by the difference in energies of electrons in the empty π^* and filled π bands, $\varepsilon_{\mathbf{k}}^{\pi^*} - \varepsilon_{\mathbf{k}}^{\pi}$ (where \mathbf{k} is the electronic wave vector), with or without the phonon energy $\hbar\Omega_{\mathbf{q}=0}$ at the phonon wave vector $\mathbf{q} = 0$ (where \hbar is Planck's constant). The decay rate of the intermediate states is given by the sum of the scattering rates of the electron in the π^* band, $2\gamma_{\mathbf{k}}^{\pi^*}/\hbar$, and of the hole in the π band, $2\gamma_{\mathbf{k}}^{\pi}/\hbar$. The contribution from the phonon decay is typically smaller.

Counterintuitively, the electronic wave vectors \mathbf{k} mostly contributing to the matrix element for the G peak are not only those for which the excitation energies $\varepsilon_{\mathbf{k}}^{\pi^*} - \varepsilon_{\mathbf{k}}^{\pi}$ lie within an interval $\sim \gamma$ from $\hbar\omega_L$ or $\hbar\omega_L - \hbar\Omega_{\mathbf{q}=0}$, where $\hbar\omega_L$ is the incident laser photon energy. Instead, they are such that $|\varepsilon_{\mathbf{k}}^{\pi^*} - \varepsilon_{\mathbf{k}}^{\pi} - \hbar\omega_L|$ can be of the order of $\hbar\omega_L$ itself, and there are strong cancellations in the sum over \mathbf{k} (ref. 52). These cancellations correspond to destructive quantum interference. In fact, this interference can be controlled externally. Indeed, occupations of electronic states can be changed by doping and, because transitions from an empty state or to a filled state are impossible due to Pauli blocking, doping can effectively exclude some regions of \mathbf{k} from contributing to the matrix element (Fig. 2a). Owing to suppression of destructive interference, this leads to an increase of the G-peak intensity at high doping levels, as was predicted by Basko⁵², and observed by Kalbac *et al.*¹⁹ and Chen *et al.*²⁰.

For two-phonon processes, the fundamental selection rule can be obeyed by any pair of phonons with opposite wave vectors, $\mathbf{q}, -\mathbf{q}$. The matrix element has four contributions corresponding to processes when (i) both phonons are emitted by the electron (ee), (ii) both phonons are emitted by the hole (hh), and (iii) one

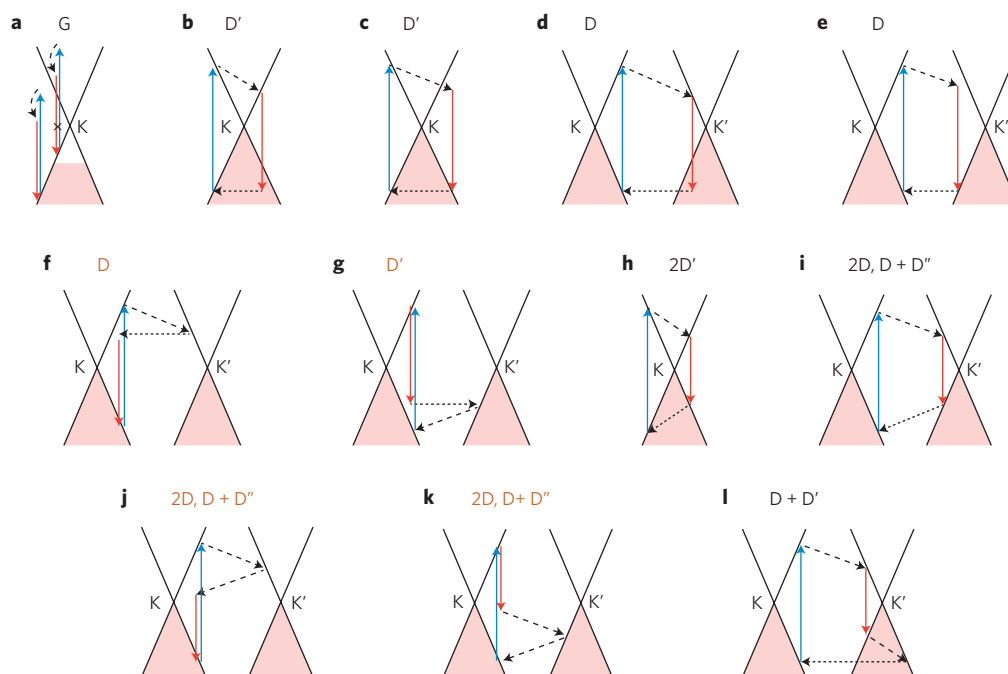


Figure 2 | Raman processes. Electron dispersion (solid black lines), occupied states (shaded areas), interband transitions neglecting the photon momentum, accompanied by photon absorption (blue arrows) and emission (red arrows), intraband transitions accompanied by phonon emission (dashed arrows), electron scattering on a defect (horizontal dotted arrows). **a**, One-phonon processes responsible for the G peak, which interfere destructively. Some processes can be eliminated by doping, such as the one that is crossed out. **b–g**, In the presence of defects, the phonon wave vector need not be zero, producing the D' peak for intravalley scattering (**b,c**), and D peak for intervalley scattering (**d–g**). Besides the eh or he processes, where the electron and the hole participate in one act of scattering each (**b–e**), there are contributions (ee, hh) where only the electron (**f**) or the hole (**g**) are scattered. **h–k**, For two-phonon scattering, momentum can be conserved by emitting two phonons with opposite wave vectors, producing the 2D' peak for intravalley scattering (**h**) and the 2D, D + D' peaks for intervalley scattering (**i–k**). The ee and hh processes are shown in **j,k,l**. With defects, one intravalley and one intervalley phonon can be emitted, producing the D + D' peak. The processes (**f,g,j,k**) give a small contribution, as indicated by the orange peak labels.

phonon is emitted by the electron, and the other by the hole (eh and he). In principle, it would be expected that the two-phonon Raman spectrum be a broad band, as determined by the sum of the phonon frequencies $\Omega_{\mathbf{q}}^{\alpha} + \Omega_{-\mathbf{q}}^{\beta}$ from branches α, β for all \mathbf{q} , with possible features from Van Hove singularities in the joint phonon density of states. However, resonance conditions favour phonon states with \mathbf{q} coupling electronic states $\mathbf{k}, \mathbf{k} - \mathbf{q}$, either in the same valley (that is, with \mathbf{q} near Γ), or in different valleys (\mathbf{q} near \mathbf{K}). But, it turns out that, even among these \mathbf{q} , very few are selected by subtle effects of resonance and quantum interference^{41,53}. These effects are captured by the direct integration over the electron momentum, where they appear as cancellations in the sum over \mathbf{k} , but they are more easily understood by considering the Raman process in real space.

Raman scattering in the real space was first studied in 1974¹⁰³, and the spatial separation between the photoexcited electron and the hole in cascade multiphonon Raman scattering was analysed in 1983¹⁰⁴. However, in the context of graphene this approach was proposed only recently^{28,31,53}. The real-space picture is especially useful when translational invariance is lacking due to defects or edges. It arises because of separation of two energy scales: the electronic energy $\varepsilon \approx \hbar\omega_1/2$ (~ 1 eV for visible Raman), and the energy uncertainty $\delta\varepsilon \ll \varepsilon$. For the triple-resonant processes in Fig. 2h,i,l, $\delta\varepsilon$ is of the order of the broadening γ (a few tens of meV; refs 41,63,88). For double-resonant processes in Fig. 2b–g,j,k, $\delta\varepsilon$ is of the order of the phonon energy, that is, 0.17 or 0.20 eV for phonons near Γ or \mathbf{K}, \mathbf{K}' (ref. 80). From the uncertainty principle, $\delta\varepsilon$ determines the typical lifetime of the intermediate state, $\sim \hbar/\delta\varepsilon$,

be it real or virtual. This gives the process duration, whereas $\ell = \hbar v_F / \delta\varepsilon$ gives its spatial extent ($v_F \approx 10^8$ cm s⁻¹ ≈ 7 eV \AA h⁻¹ is the Fermi velocity). For triple-resonant processes with $\gamma = 20$ meV, we have $\ell \sim \hbar v_F / \gamma \approx 35$ nm; for double-resonant processes, $\ell \sim v_F / \Omega \approx 3.5$ nm (for $\hbar\Omega = 0.2$ eV). As ℓ is much bigger than the electron wavelength, $\lambda_e = \hbar v_F / \varepsilon \approx 0.7$ nm for $\hbar\omega_1 = 2$ eV, the electron and hole motion can be viewed in a quasi-classical manner, as shown in Fig. 3 for two-phonon processes. This is analogous to the geometrical optics approximation for electromagnetic waves, with electronic trajectories corresponding to light rays. The quasi-classical picture arises when calculating the Raman matrix elements in the coordinate representation²⁸. It does not require real e,h populations, as it is a property of wavefunctions.

From the real-space picture it is seen that those \mathbf{q} that correspond to e and h scattered backwards (otherwise e and h will not meet in the same point) contribute the most to two-phonon processes. The backscattering condition, corresponding to reversal of the group velocity direction, agrees with the nesting condition described by Venezuela *et al.*⁴¹, and was mentioned as early as 1974¹⁰⁵. In particular, this eliminates the contribution from two phonons with $\mathbf{q} = 0$, which would correspond, for example, to the G-peak overtone, explaining why the 2G peak is not seen in the Raman spectrum (unfortunately many works still mistakenly name the 2D' peak as 2G). Also, the ee and hh processes, where one of the carriers has to travel for longer than the other, are in conflict with the requirement that they travel for the same time (this would not be the case if e and h had strongly different velocities). Strictly speaking, such processes, prohibited in

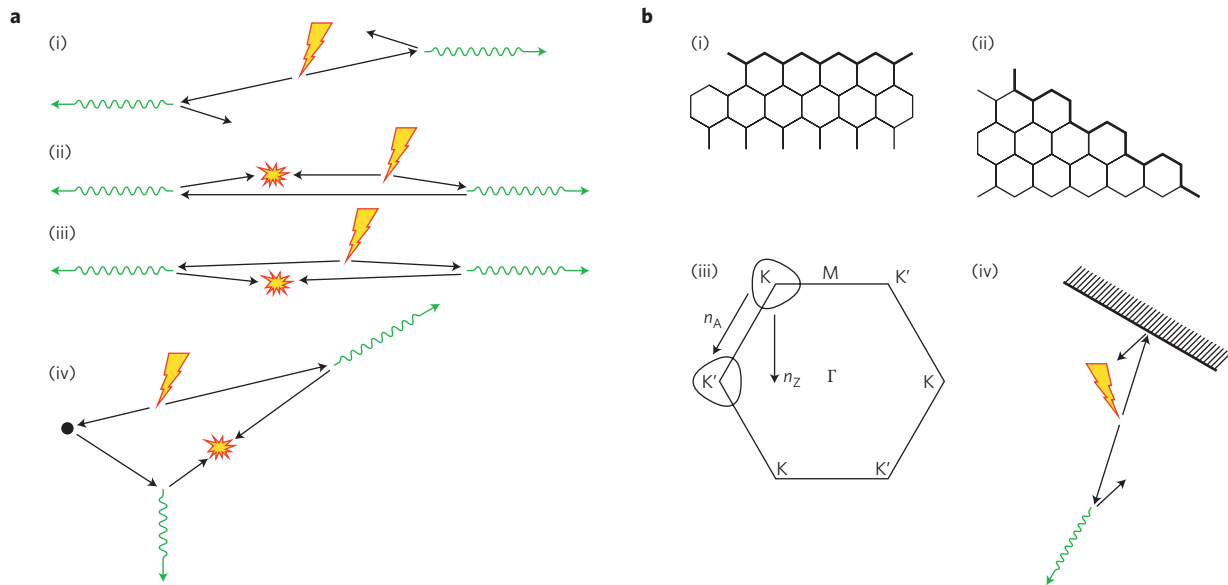


Figure 3 | Real-space Raman processes. The excitation photon promotes an electron with momentum $\mathbf{p} = \hbar\mathbf{k}$ from π to π^* , thereby creating a hole in the π band with momentum $-\mathbf{p}$, and energy $-\varepsilon_{\mathbf{k}}^{\pi}$, shown by the lightning. This process is assumed to take place in a given point in space. e and h then move along classical trajectories, in directions determined by their group velocities, $v_e^x = \partial\varepsilon_{\mathbf{k}}^{\pi^*}/\partial(\hbar k)$, $v_h^x = \partial\varepsilon_{\mathbf{k}}^{\pi}/\partial(\hbar k)$, as shown by the black arrows. At some point, they emit phonons (green wavy lines) or scatter on defects (black dots) or edges (hatched zones). To recombine radiatively and produce the scattered photon (flash), e and h must meet with opposite momenta \mathbf{k}' , $-\mathbf{k}'$ at the same point in space, after having travelled for the same amount of time. **a**, Trajectories for two-phonon processes. (i) Trajectory for which radiative recombination is impossible, even though momentum is conserved, because e and h cannot meet at the same point to recombine. (ii) Trajectory corresponding to an ee process, incompatible with the requirement that e and h travel for the same amount of time. (iii) Trajectory corresponding to $2D$, $2D'$. On phonon emission, e and h must be back-scattered. (iv) Trajectory corresponding to $D + D'$. **b**, Scattering at edges. (i) Zigzag edge. (ii) Armchair edge. (iii) Equi-energy contours for electronic states involved in the D peak. n_z and n_A indicate directions normal to zigzag and armchair edges, respectively. (iv) Trajectory not contributing to D , as e and h cannot meet after scattering.

the classical picture (corresponding to $\delta\varepsilon/\varepsilon \rightarrow 0$), are allowed in the full quantum picture, but are weaker than the dominant contribution. Note that the G peak is also classically forbidden (e and h cannot meet at the same point). Thus, one may wonder why it produces a noticeable feature, while classically forbidden processes in two-phonon scattering are not seen. One reason is that two-phonon processes contain a higher power of the small electron-phonon coupling (EPC); another is that the G peak is narrow (a few cm^{-1}), whereas the two-phonon bands are spread over hundreds of cm^{-1} .

In samples with defects the overall momentum conservation can be satisfied by adding an electron-defect scattering event to the process. We can thus have (i) one-phonon defect-assisted processes, producing the D , D' , D'' and other smaller peaks, and (ii) two-phonon defect-assisted processes, such as those leading to the $D + D'$ peak. For one-phonon defect-assisted processes the matrix element has the same form as two-phonon defect-free processes. It is sufficient to replace the electron-phonon Hamiltonian by the electron-defect Hamiltonian, and set the frequency of the second phonon to zero. For the two-phonon defect-assisted processes the situation is quite different. The explicit formula for the matrix element contains 48 terms, each having five matrix elements in the numerator and a product of four factors in the denominator. Figure 3a(iv) shows that for the $D + D'$ peak there is no backscattering restriction, so the phonon momenta (counted from \mathbf{K} and Γ) can be between 0 and $\omega_L/(2v_F)$. Thus, the $D + D'$ peak is much broader than the $2D$ or $2D'$ peaks, because in the latter the magnitude of the phonon momentum is fixed by the backscattering condition, and $\text{Pos}(D + D') \neq \text{Pos}(D) + \text{Pos}(D')$. Unfortunately, the $D + D'$ peak is often labelled as $D + G$ in literature, due to the lack of understanding of this activation mechanism.

These simple considerations can explain the peaks' dispersions. For example, in the $2D$ process (Fig. 2i) the photon creates e and h with momenta \mathbf{p} and $-\mathbf{p}$, counted from the Dirac points. These then emit phonons with momenta $\hbar\mathbf{q} = \mathbf{p} - \mathbf{p}'$ and $-\hbar\mathbf{q}$ (counted from the \mathbf{K} point). In the Dirac approximation for the electronic dispersion, $\varepsilon_{\mathbf{K}+\mathbf{p}/\hbar}^{\pi^*} = -\varepsilon_{\mathbf{K}+\mathbf{p}/\hbar}^{\pi} = v_F|\mathbf{p}|$, and assuming isotropic phonon dispersions around \mathbf{K} , the magnitudes of \mathbf{p} and \mathbf{p}' before and after phonon emission are fixed by the resonance condition: $2v_F p = \hbar\omega_L$, $2v_F p' = \hbar\omega_L - 2\hbar\Omega_q^{\text{TO}}$. The backscattering condition (Fig. 3a) fixes the relative orientation of \mathbf{p}, \mathbf{p}' (that is, opposite directions), thus the magnitude of \mathbf{q} :

$$q = \frac{p + p'}{\hbar} = \frac{\omega_L}{2v_F} + \frac{\omega_L - 2\Omega_q^{\text{TO}}}{2v_F} \quad (2)$$

Neglecting Ω_q^{TO} , we estimate $\text{Disp}(2D)$ as:

$$\text{Disp}(2D) = \frac{d\text{Pos}(2D)}{d\omega_L} = 2 \frac{d\Omega_q^{\text{TO}}}{dq} \frac{dq}{d\omega_L} \approx 2 \frac{v_q^{\text{TO}}}{v_F} \quad (3)$$

where $v_q^{\text{TO}} \equiv d\Omega_q^{\text{TO}}/dq$ is the TO phonon group velocity. As $d\text{Pos}(2D)/d\omega_L \approx 100 \text{ cm}^{-1} \text{ eV}^{-1}$ (ref. 106), we obtain $v_q^{\text{TO}} \approx 0.006v_F$. A similar argument holds for the $D + D''$ peak, whose experimentally observed $\text{Disp}(D + D'') \approx -20 \text{ cm}^{-1} \text{ eV}^{-1}$, is determined as $v_q^{\text{TO}}/v_F + v_q^{\text{LA}}/v_F$ (the LA phonon has a negative slope as the wave vector moves away from the \mathbf{K} point)^{55,107}.

An understanding of the main contributions to the widths of the Raman peaks in the spectra of graphene has recently been achieved. Besides the anharmonic and EPC contributions, which

dominate the width of the G peak^{25,26,50}, other factors can contribute to the widths of higher-order peaks. One is the e,h dispersion anisotropy, as phonons emitted by electrons with different **p** directions have different frequencies⁴¹. Another is electronic momentum uncertainty due to the electronic scattering rate^{53,63}. When all these mechanisms are taken into account (note that they are not simply additive), the experimental width of the peaks, such as D and 2D, is reproduced⁴¹.

The intensities of the two-phonon peaks are suppressed by electronic scattering^{41,53}. Anisotropy of the latter^{108,109}, together with the EPC anisotropy⁴¹, makes the electronic states close to the K–M line (the so-called inner resonance) dominate the two-phonon Raman process, which explains recent experimental observations^{34–36,110}.

For the D and D' peaks, the electron and hole momenta can have different magnitudes, depending on which of the intermediate states is virtual¹¹¹, as shown in Fig. 2d,e. Arguments analogous to those presented above give two possibilities for the emitted phonon momentum: $q = \omega_L/\nu_F$ and $q = (\omega_L - \Omega_q^v)/\nu_F$. This means that the D peak could, in principle, have two components¹¹¹ separated by $(\nu_q^{\text{TO}}/\nu_F)\Omega_q^{\text{TO}} \approx 8 \text{ cm}^{-1}$ (not to be confused with the two D-peak components in graphite⁸⁹, which reflect the three-dimensional electron branches¹² (see below), or with the broadening and splitting expected for ultraviolet excitation). Such splitting, if present, should be seen in the Raman spectrum. However even in SLG with very few defects, FWHM(D) is $\sim 20 \text{ cm}^{-1}$, thus larger than this splitting. This also means that Pos(D) can be slightly higher than $(1/2)\text{Pos}(2D)$, as the latter is uniquely determined by $q_{2D} = (\omega_L - \Omega_q^{\text{TO}})/\nu_F$. For D', $(\nu_q^{\text{LO}}/\nu_F)\Omega_q^{\text{TO}} \sim 2 \text{ cm}^{-1}$, thus the difference between Pos(2D') and 2 Pos(D') is barely detectable.

The intensities of different peaks were reported to depend differently on the excitation frequency ω_L (ref. 112): whereas A(D), A(D'), A(2D) show no ω_L dependence, A(G) was found to be $\propto \omega_L^4$. The independence of A(2D) on ω_L agrees with the theoretical prediction⁵³ if one assumes that the electronic scattering rate is proportional to the energy. For the G peak, ref. 52 predicts $A(G) \propto \omega_L^2$ at low ω_L , and strong enhancement of A(G) as ω_L approaches the Van Hove singularity corresponding to the electronic excitation at the M point, reported to be as low as 4.6 eV (refs 113,114). It cannot be excluded that the ω_L^4 dependence, established empirically from measurements in the range $\omega_L = 1.6\text{--}2.7 \text{ eV}$, corresponds to the crossover between ω_L^2 and the enhancement at the Van Hove singularity. For the D peak, ref. 28 gives $A(D) \propto \omega_L$. The reason for the discrepancy with experiments remains unclear. Note, however, that a fully quantitative theory for A(D) and its excitation energy dependence is not trivial because, in general, A(D) depends not only on the concentration of defects, but on their type as well (for example, only defects able to scatter electrons between the two valleys can contribute). Different defects can also produce different frequency and polarization dependence of A(D). Thus a wealth of information still remains to be uncovered from the D peak.

So far, we only considered Stokes processes. For anti-Stokes processes the resonance conditions are modified. For the 2D peak, the momentum of the absorbed phonons is determined by an equation similar to equation (2), but with a '+' sign in front of $2\Omega_q^{\text{TO}}$. Thus, the phonon momenta in the anti-Stokes process are greater than Stokes processes by $2\Omega_q^{\text{TO}}/\nu_F$. This explains the Stokes/anti-Stokes processes difference^{91,92,111}:

$$\text{Pos}(2D)_{\text{AS}} - \text{Pos}(2D)_{\text{S}} \approx 4\Omega_q^{\text{TO}} \frac{\nu_q^{\text{TO}}}{\nu_F} \approx 34 \text{ cm}^{-1} \quad (4)$$

where AS is the anti-Stokes and S is the Stokes process.

As discussed above the D, D' peaks could, in principle, have two components. In this case, one of them would have the same

frequency in the Stokes and anti-Stokes scattering, while the other would correspond to a lower frequency in Stokes, and a higher one in anti-Stokes (ref. 111).

It is important to consider the Stokes/anti-Stokes difference when determining the temperature (*T*) from the Stokes/anti-Stokes ratio, both in nanotubes and graphene, as the phonons involved in Stokes and anti-Stokes are not the same, unlike what generally happens in other materials, and contrary to what is required for determining *T* from this ratio. Accurate calibrations are thus needed. It should come as no surprise if a mismatch between expected and measured *T* arises.

Edges

Edges are preferred sites to attach functional groups¹¹⁵, and their electronic and magnetic properties are different from the bulk¹¹⁵. Figure 3b(i,ii) shows zigzag and armchair edges schematically. There is evidence that such ideal edges can be produced by chemical¹¹⁶ or thermal treatments¹¹⁷. However, most exfoliated samples, even if with macroscopically smooth edges oriented at well-defined angles, are in fact not necessarily microscopically ordered, with disordered edges, often consisting of zigzag and armchair segments^{117,118}.

Edges can be viewed as extended defects, breaking the translational symmetry, even though a perfect zigzag or armchair edge still preserves the translation symmetry along the edge. An immediate consequence of symmetry breaking is the D,D' peak activation. However, a closer look at the Raman process shows that a perfect zigzag edge cannot produce a D peak^{29,31,119}. Indeed, due to translational invariance along the edge, a perfect zigzag edge cannot scatter electrons between the **K** and **K'** valleys (Fig. 3b(iii)). This does not apply to the D' peak. This peak, not involving intervalley scattering, can be activated both by armchair and zigzag edges, as the normal vectors to both edges **n_z**, **n_A** are compatible with the required intravalley scattering. This is not enough to determine whether one type of edge is more efficient than the other for D'-peak activation.

In the real space, a perfect armchair edge requires the electronic momentum to be perpendicular to it, to contribute to D, otherwise e and h cannot meet and recombine radiatively (Fig. 3b(iv)). Thus, **k** needs to be along $\Gamma\text{--K--M}$ to contribute to D. This, in combination with the $[\mathbf{e} \times \mathbf{k}]$ dependence for the dipole transition matrix element (**e** being the polarization vector), discussed in Supplementary Section S5, results in a strong polarization dependence: $I(D) \propto \cos^2\theta$, if the excitation is performed with linearly polarized light, oriented at an angle θ with respect to the edge, and all polarizations are detected for the scattered light, or $I(D) \propto \cos^4\theta$ if an analyser, parallel to the polarizer, is used. For the D' peak the real-space picture is analogous to that for the D peak. For regular edges this leads to the same $I(D') \propto \cos^2\theta$ or $\cos^4\theta$ dependence, as observed in refs 29–31,119.

For a disordered edge, $I(D)$ and $I(D')$ do not vanish even for $\theta = \pi/2$ (polarization **e** perpendicular to the edge). Indeed, the polarization dependence for a disordered edge is determined by contributions from armchair and zigzag segments with different orientations. The ratio $I(D)_{\text{min}}/I(D)_{\text{max}}$ can be used as a measure of edge imperfection³¹.

The G peak, even though present in the bulk, can be modified near an edge. The edge changes the electronic states, which affects (i) the EPC correction to the phonon frequency, and (ii) electron–phonon and electron–photon matrix elements, responsible for the Raman process itself¹²⁰. The correction to the phonon frequency vanishes for displacements perpendicular to the zigzag or armchair edge. The electron–phonon and electron–photon matrix elements vanish when displacements or light polarization are parallel (perpendicular) to the zigzag (armchair) edge. Thus, one of the two modes (depending on edge type) does not show

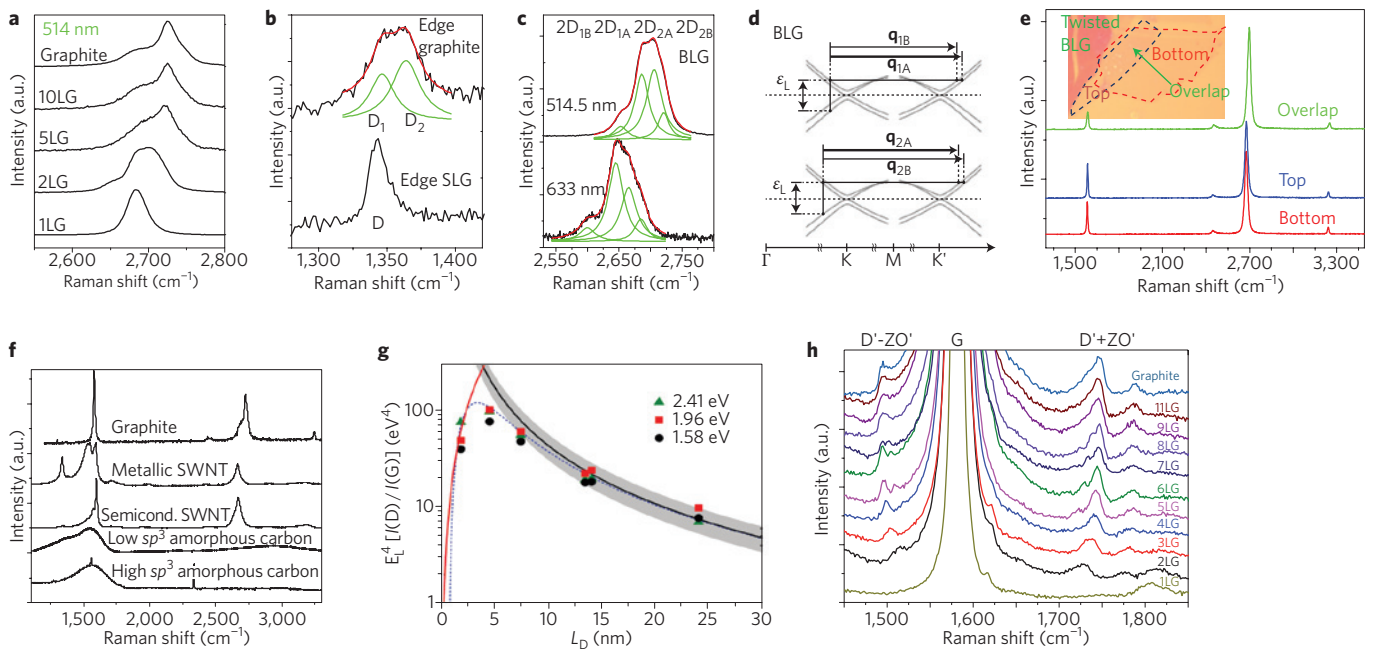


Figure 4 | Dependence of the Raman spectra on number of layers and disorder. **a**, 2D peak as a function of N for 514 nm excitation. Flakes are labelled as in Fig. 1f. **b**, D peak at the edge of graphite and SLG. **c**, 2D peak of BLG measured at 514.5 nm and 633 nm. In **b,c** the red curves show multiple Lorentzian fits, and the green curves show the individual Lorentzian components, labelled by D with corresponding subscripts. **d**, Phonon wave vectors corresponding to the 2D peak in BLG. **e**, Raman spectra of two individual SLGs juxtaposed to create a twisted BLG. The inset shows the sample. **f**, Raman spectra of graphite, metallic and semiconducting nanotubes, low and high sp^3 amorphous carbons. **g**, Amorphisation trajectory $E_1^4 [I(D)/I(G)]$ as a function of L_D for different excitation energies E_L (refs 15,16,43). The dashed blue line is obtained from the empirical model of ref. 42. The solid black and red lines are L_D^{-2} and L_D^2 dependences, respectively. The shaded area accounts for the upper and lower limits given by the 30% experimental error. **h**, Combination modes close to the G peak as a function of N . Flakes are labelled as in Fig. 1f. The peaks at $-1,500 \text{ cm}^{-1}$ and between $-1,700 \text{ cm}^{-1}$ and $-1,840 \text{ cm}^{-1}$ are assigned as the anti-Stokes and Stokes combinations of the E_{2g} LO phonon and the B_{2g} ZO' phonon (layer-breathing mode), respectively^{70,72}. Panels **a-d** reproduced from ref. 12, © 2006 APS.

a Kohn anomaly, and does not contribute to the Raman spectrum. This produces (i) a dependence of $I(G)$ on the laser spot location¹²⁰; (ii) strong polarization dependence of $I(G)$ near the edge: $I(G) \propto \cos^2\theta$ for a perfect armchair and $I(G) \propto \sin^2\theta$ for a perfect zigzag edge, allowing the edge type to be probed³² and even controlled¹²¹.

Number and relative orientation of layers

There is a significant change in the shape and intensity of the 2D peak when moving from SLG to graphite¹² (Fig. 4a). The same holds true for the D peak, as shown in Fig. 4b, where the D peak at an SLG edge is compared to that at a graphite edge. The 2D peak in graphite has two components $2D_1$ and $2D_2$ (refs 89,106), roughly 1/4 and 1/2 of $I(G)$. Figure 4a plots the evolution of the 2D peak as a function of N for 514.5-nm and 633-nm excitations¹². Figure 4c shows that BLG has a different 2D peak compared with both SLG and graphite¹². It has four components, $2D_{1B}$, $2D_{1A}$, $2D_{2A}$, $2D_{2B}$, two of which, $2D_{1A}$ and $2D_{2A}$, have higher intensities. For $N > 5$ the spectrum is hardly distinguishable from graphite. We note that Faugeras *et al.*⁶⁴ used the evolution of the G peak in a strong magnetic field to identify a four-layer sample.

The evolution of the electronic bands with N explains the 2D peak change¹². In BLG, the interaction of the graphene planes causes the π and π^* bands to divide in four, with a different splitting for e and h (Fig. 4d). The incident light couples only two pairs of the four bands (Fig. 4d). On the contrary, the two almost degenerate TO phonons can couple all bands. The resulting four processes involve phonons with momenta \mathbf{q}_{1B} , \mathbf{q}_{1A} , \mathbf{q}_{2A} , \mathbf{q}_{2B}

(Fig. 4d). \mathbf{q}_{1A} , \mathbf{q}_{2A} link bands of the same type and are associated with processes more intense than \mathbf{q}_{1B} , \mathbf{q}_{2B} , because the portion of the phase space where triple resonance is satisfied is larger. These correspond to different frequencies, due to the phonon dispersion around K (Fig. 1d) (ref. 80). This gives four peaks in BLG (ref. 12). Their excitation-energy dependence is determined by both electron and phonon dispersions. Measuring it probes the interlayer coupling for both^{107,122}.

We now examine bulk graphite^{12,123}. In this case the electronic energy depends on the wave vector along the (001) direction, k_{\perp} . For a fixed k_{\perp} , the in-plane dispersion is similar to that of BLG, with the splitting between the branches depending on k_{\perp} . In principle, the excited phonons can have any perpendicular wave vector \mathbf{q}_{\perp} , however, the main contribution comes from the one-dimensional Van Hove singularity at $\mathbf{q}_{\perp} = 0$. The resulting in-plane phonon momenta \mathbf{q}_{1B} , \mathbf{q}_{1A} , \mathbf{q}_{2A} , \mathbf{q}_{2B} depend on k_{\perp} of the excited electron and hole. Summation over all possible k_{\perp} gives a distribution of allowed \mathbf{q} 's, in turn associated with a Raman frequency distribution. The lower branch of the graphite electronic dispersion has weaker dependence on k_{\perp} than the upper one. Thus, also \mathbf{q}_{2B} , corresponding to the only process not involving the upper branch, has weaker dependence on k_{\perp} than \mathbf{q}_{1B} , \mathbf{q}_{1A} , \mathbf{q}_{2A} . As a result, $2D_{2B}$ appears as a sharp peak, whereas others merge into a low-frequency shoulder.

Not all multilayers are Bernal stacked. In fact, it is possible to observe more complex 2D peak shapes than those described thus far, for example, in samples grown by carbon segregation or chemical vapour deposition, as well as combinations in bulk or exfoliated

samples^{65,124}. In principle, any relative orientation and stacking of the graphene layers could be possible, and this would be reflected in a significant change of the band structure⁹⁶. Indeed, some orientations and stackings do result in a Dirac-like spectrum⁹⁶, thus giving a SLG-like 2D peak, even in few-layer graphene (FLG). It was noted in early studies that turbostratic graphite has a single 2D peak¹²⁵, but with FWHM(2D) almost double than SLG, and Pos(2D) upshifted by $\sim 20 \text{ cm}^{-1}$. Turbostratic graphite often has a D peak¹²⁵, thus defect-induced broadening. It is possible to prepare multilayers with any relative orientation^{4,5}. Figure 4e compares the spectra of two SLGs and a BLG formed by their juxtaposition. The SLG 2D peak shape is preserved in the twisted BLG. Thus, a detailed study of the 2D peak shape can bear important information on the multilayer interactions, and the presence of Dirac electrons in FLG^{65,124}. On the other hand, especially when characterizing grown samples, care should be taken in asserting that a single Lorentzian 2D peak is proof of SLG. This could also be consistent with turbostratic or twisted FLG, especially if broader than in exfoliated SLG. By carefully studying the shape and width of the 2D band, it is then possible to distinguish between different stackings¹²⁶ and relative orientations¹²⁷. Another signature of twisted BLGs is the appearance of two one-phonon peaks, one in the region 1,350–1,550 cm^{-1} , and the other around 1,620 cm^{-1} . These peaks, non-dispersive with ω_L , are due to phonons whose wave vectors are determined by the period of the superlattice that is formed by the superposition of the two SLGs and that relaxes the fundamental selection rule $\mathbf{q} = 0$ (refs 128,129).

It is also interesting to note that single-walled nanotubes show a sharp 2D peak, similar to SLG (ref. 130), whereas double or multiple peaks can be observed in multi-walled tubes¹³¹. Their shape and position bears information on the interaction and relative orientation of each tube, and their diameters.

As discussed earlier, another method to probe N and stacking order in multilayer graphene is based on Raman signatures of out-of-plane vibrations^{69–72}. In SLG, the two out-of-plane modes A_{2u} and B_{2g} (Fig. 1b) are not Raman active. Figure 4h shows that close to the G peak there are other features scaling in position with N . Of interest is the peak between 1,700 and 1,750 cm^{-1} assigned to the Stokes combination of the E_{2g} LO phonon and the B_{2g} ZO' phonon LBMs^{69,72}. This corresponds to a double resonant process and its frequency depends on the laser excitation energy E_L . Its anti-Stokes combination can also be seen in Fig. 4h below the G peak. Moreover, in FLG this splits into several components, as the number of LBMs and their frequencies depend on N and on the stacking order. The C peak also bears direct information on interlayer coupling, scaling with N (Fig. 1f) (ref. 68). Note that, even though the 2D shape reflects the change in the band structure with N (and this very change is what allows N to be determined), the phonons involved are always in-plane, whereas the C and LBM phonons involve the relative motion of the planes, thus are a direct probe of layering.

Defects and disorder

Quantifying defects in graphene related systems, which include a large family of sp^2 carbon structures, is crucial both to gain insight in their fundamental properties, and for applications. In graphene, this is a key step towards the understanding of the limits to its ultimate mobility^{47,48,132}.

Ferrari and Robertson¹⁵ introduced a three stage classification of disorder that, leading from graphite to amorphous carbons, allows all Raman spectra of carbons to be assessed simply: (1) Graphite to nanocrystalline graphite; (2) nanocrystalline graphite to low sp^3 amorphous carbon; (3) low sp^3 amorphous carbon to high sp^3 amorphous carbon. In the study of graphene, stages 1 and 2 are the most relevant and summarized here.

In stage 1 the spectrum evolves as follows¹⁵: (a) a D peak appears and $I(D)/I(G)$ increases; (b) a D' peak appears; (c) all

peaks broaden, so that the D and 2D peaks lose their doublet structure in graphite; (d) the D + D' peak appears; (e) at the end of stage 1, the G and D' peaks are so wide that it is sometimes more convenient to consider them as a single, upshifted, wide G band at $\sim 1,600 \text{ cm}^{-1}$.

In their seminal work, Tuinstra and Koenig noted that $I(D)/I(G)$ varied inversely with the crystal size, L_a : $I(D)/I(G) = C(\lambda)/L_a$, where the coefficient $C(514 \text{ nm}) \sim 4.4 \text{ nm}$ (refs 11,133,134) ($\lambda = 2\pi c/\omega_L$ is the excitation wavelength). Initially, this was understood in terms of phonon confinement: the intensity of the forbidden process would be ruled by the 'amount of lifting' of the selection rule¹¹, $\Delta q \propto 1/\Delta x$, where the coordinate uncertainty $\Delta x \approx L_a$. Now, it is understood theoretically and established experimentally, that the D peak is produced only in a small region of the crystal (size $\sim v_L/\Omega^{\text{TO}} \sim 3\text{--}4 \text{ nm}$) near a defect or an edge^{28,31,42,135}. For a nanocrystallite, $I(G)$ is proportional to the sample area, $\propto L_a^2$, whereas $I(D)$ is proportional to the overall length of the edge, which scales as L_a . Thus, $I(D)/I(G) \propto 1/L_a$. For a sample with rare defects, $I(D)$ is proportional to the total number of defects probed by the laser spot. Thus, for an average inter-defect distance L_D , and laser spot size L_L , there are on average $(L_L/L_D)^2$ defects in the area probed by the laser, thus $I(D) \propto (L_L/L_D)^2$. On the other hand, $I(G)$ is proportional to the total area probed by the laser $\propto L_L^2$, thus $I(D)/I(G) = C''(\lambda)/L_D^2$. For very small L_D , one must have $C''(\lambda)/L_D^2 = I(D)/I(G) = C(\lambda)/L_a$. This condition gives an estimate of $C''(514 \text{ nm}) \sim 90 \text{ nm}$. Lucchese *et al.*⁴² measured $I(D)/I(G)$ for irradiated SLG with known L_D , derived from scanning tunnelling microscopy, obtaining $I(D)/I(G) \approx 145/L_D^2$ at 514 nm excitation, in excellent agreement with this simple estimate (Fig. 4g).

For an increasing number of defects, the Tuinstra and Koenig relation, in either form, must eventually fail¹⁵. The 'molecular' picture outlined in Supplementary Section S4 helps us understand what happens¹⁵. For high disorder, sp^2 clusters become smaller and the rings become fewer and more distorted, until they open up. As the G peak is just related to the relative motion of sp^2 carbons, we can assume $I(G)$ to be roughly constant as a function of disorder. Thus, with the loss of sp^2 rings, $I(D)$ will now decrease with respect to $I(G)$ and the Tuinstra and Koenig relation will no longer hold. For very small L_a or L_D , the D mode strength is proportional to the number of 6-fold rings in the laser spot¹⁵. Thus, in amorphous carbons the development of a D peak indicates ordering, exactly the opposite to graphene¹⁵. The proportionality of $I(D)/I(G)$ to the number of rings leads to a new relation for stage 2: $I(D)/I(G) = C'(\lambda)L_a^2$. Imposing continuity with the Tuinstra and Koenig relation at $L_a = 3 \text{ nm}$ gives $C'(514 \text{ nm}) \sim 0.55$ (ref. 15) (Fig. 4g).

The spectrum in stage 2 evolves as follows¹⁵: (a) Pos(G) decreases from $\sim 1,600 \text{ cm}^{-1}$ towards $\sim 1,510 \text{ cm}^{-1}$; (b) the Tuinstra and Koenig relation fails; $I(D)/I(G) \rightarrow 0$; (c) Pos(G) acquires a dispersion as a function of excitation energy, the bigger the stronger the disorder; (d) there are no more well-defined second-order peaks, but a small modulated bump between 2,300 and $\sim 3,200 \text{ cm}^{-1}$ (Fig. 4f).

In disordered carbons Pos(G) increases as the excitation wavelength decreases, from the infrared to ultraviolet¹⁶. Disp(G) increases with disorder. This separates the materials into two types. In those with only sp^2 rings, Disp(G) saturates at $\sim 1,600 \text{ cm}^{-1}$, that is Pos(G) at the end of stage 1. In contrast, for those containing sp^2 chains (such as in amorphous and diamond-like carbons), Pos(G) continues to rise past $1,600 \text{ cm}^{-1}$ and can reach $1,690 \text{ cm}^{-1}$ for 229 nm excitation¹⁶.

The D peak always disperses with excitation energy, however, the higher the disorder, the lower Disp(D), opposite to G (ref. 16). Finally, FWHM(G) always increases with disorder¹³⁶. Thus, combining $I(D)/I(G)$ and FWHM(G) allows stages 1 or 2 to

be discriminated between, because samples in stage 1 and 2 could have the same $I(D)/I(G)$, but not the same $\text{FWHM}(G)$, being this much bigger in stage 2 (refs 136,43).

It is important to understand what the maximum in Fig. 4g means. $I(D)$ increases as long as the contributions from different defects add up independently. However, if two defects are closer than the average distance an electron-hole pair travels before scattering with a phonon, then their contributions will not sum anymore. Above we estimated it as $v_F/\omega_D \sim 3.5$ nm. This is in agreement with the predictions of Ferrari and Robertson¹⁵ and measurements of Lucchese *et al.*⁴² and Cançado *et al.*⁴³.

The excitation-energy dependence of the peaks areas and intensities, discussed above, can be exploited to generalize the amorphisation trajectory for any visible excitation energy. Figure 4g plots $E_L^4 [I(D)/I(G)]$ as a function of L_D , as measured in ref. 43, where $E_L = \hbar\omega_L$ is the laser excitation energy in eV. The data with $L_D > 10$ nm, obtained with different laser energies, collapse in the same curve. In this regime the D-band scattering is proportional to the number of point defects, giving rise to $I(D)/I(G) \propto 1/L_D^2$, as discussed above. A fit to the experimental data gives⁴³:

$$L_D^2 (\text{nm}^2) = \frac{4.3 \times 10^3}{E_L^4 (\text{eV}^4)} \left[\frac{I(D)}{I(G)} \right]^{-1} \quad (5)$$

In terms of defect density $n_D^2 = 1/(\pi L_D^2)$, or $n_D (\text{cm}^{-2}) = 10^{14}/(\pi L_D^2)$:

$$n_D^2 (\text{cm}^{-2}) = 7.3 \times 10^{-9} E_L^4 (\text{eV}^4) \frac{I(D)}{I(G)} \quad (6)$$

For the high defect density regime (stage 2, with $L_D < 3$ nm), $I(D)$ decreases with respect to $I(G)$ as L_D decreases, leading to $I(D)/I(G) \propto L_D^2$ (ref. 15). The red line in Fig. 4g is the fit to the data with $L_D < 3$ nm giving:

$$L_D^2 (\text{nm}^2) = 5.4 \times 10^{-2} E_L^4 (\text{eV}^4) \frac{I(D)}{I(G)} \quad (7)$$

$$n_D^2 (\text{cm}^{-2}) = \frac{5.9 \times 10^{14}}{E_L^4 (\text{eV}^4)} \left[\frac{I(D)}{I(G)} \right]^{-1} \quad (8)$$

The proportionality factor in equation (7) at 2.41 eV is $\sim(0.55)^{-1}$, in excellent agreement with that proposed by Ferrari and Robertson¹⁵.

Note that these relations are of course limited to Raman active defects in undoped samples. For example, perfect zigzag edges^{120,31}, charged impurities^{21,22}, intercalants²³, uniaxial and biaxial strain^{37,39} do not generate a D peak. For these types of 'silent' defects, other Raman signatures can be used. A perfect zigzag edge does change the G-peak shape^{121,32}, whereas strain, intercalants and charged impurities have a strong influence on the G and 2D peaks^{21–23,37}. In this case, the combination of Raman spectroscopy with other independent probes of the number of defects can provide a wealth of information on the nature of such defects.

Effect of perturbations

The Raman spectrum of graphene is quite sensitive to changes in many external parameters, such as strain, gate voltage, magnetic field and so on, making it a powerful and useful characterization tool. These can modify (i) the phonon properties (that is, their energies and decay rates), or (ii) the Raman process itself. Effects of the first type can only change positions and widths, not frequency-integrated intensities, because the total spectral weight of each phonon state is conserved under perturbations. Thus, by

studying peak areas and their dependence on various parameters one can extract detailed information on the Raman process, in particular on the electronic excitations, which are intermediate states. This is especially true for triple-resonant processes, among which the 2D process is the most convenient to analyse. The 2D' process will be analogous to the 2D process in most situations, but the 2D peak is more intense due to Coulomb-induced EPC enhancement^{51,56,88}. Supplementary Sections S6–S10 overview the effect of various types of perturbation on the Raman spectra: electric field and doping (Supplementary Section S6), magnetic field (Supplementary Section S7), uniaxial and biaxial strain (Supplementary Section S8), temperature (Supplementary Section S9), isotopic composition (Supplementary Section S10).

Beyond graphene

The quest to understand the Raman spectrum of graphite started over 40 years ago¹¹. This may be the longest any Raman spectrum has been studied for, and is bound to continue for years to come. The availability of monolayer graphene widened even more, if at all possible, the appeal of this technique. The study of Raman scattering in other layered materials has just begun. We note that the seminal work of Novoselov *et al.*¹³⁷ not only indicated how to produce graphene by micromechanical cleavage, but also reported layers of other materials, such as MoS₂. The Raman spectra of the bulk counterparts of these materials were studied many years ago, often by the same authors interested in graphite, such as Nemanich *et al.* for boron nitride (ref. 138). Now that individual monolayers and multilayers are available, there is a resurgence of Raman studies on them. Many of these are polar materials, thus will behave differently from graphene as a function of N , as indicated in ref. 139 for boron nitride. Also, some of them have a wide bandgap and would benefit from ultraviolet Raman measurements to reach resonance¹⁴⁰. The current interest in topological insulators, especially based on materials like BiSe, BiTe, finds in Raman spectroscopy¹⁴¹ an obvious means to probe phonon and electron interactions in these materials down to their individual units (for example, a quintuplet in the case of BiSe). Thus far, MoS₂ is one of the most studied by Raman spectroscopy among the above-mentioned materials. The Raman spectrum of bulk MoS₂ consists of two main peaks at ~ 382 and ~ 407 cm⁻¹ assigned to the E_{2g}¹ in-plane and A_{1g} out-of-plane modes, respectively¹⁴². The former redshifts, whereas the latter blueshifts with N (ref. 143). Moreover, they have opposite trends when going from bulk MoS₂ to single-layer MoS₂, so that their difference can be used to monitor N (ref. 143). However, the trends are not fully understood and more work is needed to clarify the changes with N . Raman spectroscopy of C and LBMs is also a useful tool to probe these materials. These modes change with N , with different scaling for odd and even N (ref. 95). The combinations of two-dimensional crystals in three-dimensional stacks could offer huge opportunities in designing the functionalities of such heterostructures^{5,144}. One could combine conductive, insulating, superconducting and magnetic two-dimensional crystals, tuning the performance of the resulting material¹⁴⁴, the functionality being embedded in the design of such heterostructures¹⁴⁴. Layered materials can be exploited for the realization of heterostructures. The interactions between different layers inside heterostructures and hybrids is expected to be weak if van der Waals forces hold them together. In this case, the vibrations of heterostructures and hybrids will consist of those from the individual building blocks. Therefore, Raman spectroscopy will be a useful tool for probing the stoichiometry of heterostructures and hybrids.

Received 23 August 2010; accepted 1 March 2013; published online 4 April 2013

References

- Novoselov, K. S. *et al.* Electric field effect in atomically thin carbon films. *Science* **306**, 666–669 (2004).
- Geim, A. K. & Novoselov, K. S. The rise of graphene. *Nature Mater.* **6**, 183–191 (2007).
- Charlier, J. C., Eklund, P. C., Zhu, J. & Ferrari, A. C. Electron and phonon properties of graphene: Their relationship with carbon nanotubes. *Topics Appl. Phys.* **111**, 673–709 (2008).
- Bonaccorso, F., Sun, Z., Hasan, T. & Ferrari, A. C. Graphene photonics and optoelectronics. *Nature Photon.* **4**, 611–622 (2010).
- Bonaccorso, F., Lombardo, A., Hasan, T., Sun, Z., Colombo, L. & Ferrari, A. C. Production and processing of graphene and 2d crystals. *Materials Today* **15**, 564–589 (December, 2012).
- Lin, Y. M. *et al.* 100-GHz transistors from wafer-scale epitaxial graphene. *Science* **327**, 662 (2010).
- Torrisi, F. *et al.* Inkjet-printed graphene electronics. *ACS Nano* **6**, 2992–3006 (2012).
- Sun, Z. *et al.* Graphene mode-locked ultrafast laser. *ACS Nano* **4**, 803–810 (2009).
- Landsberg, G. S. & Mandelshtam, L. I. *Eine neue Erscheinung bei der Lichtzerstreuung in Kristallen. Naturwissenschaften* **16**, 557 (1928).
- Raman, C. V. & Krishnan, K. S. A new type of secondary radiation. *Nature* **121**, 501–502 (1928).
- Tuinstra, F. & Koenig, J. L. Raman spectrum of graphite. *J. Chem. Phys.* **53**, 1126–1130 (1970).
- Ferrari, A. C. *et al.* Raman spectrum of graphene and graphene layers. *Phys. Rev. Lett.* **97**, 187401 (2006).
- Ferrari, A. C. & Robertson, J. (eds) Raman spectroscopy in carbons: from nanotubes to diamond, Theme Issue, *Phil. Trans. R. Soc. A* **362**, 2267–2565 (2004).
- Ferrari, A. C. Raman spectroscopy of graphene and graphite: Disorder, electron-phonon coupling, doping and nonadiabatic effects. *Solid State Comm.* **143**, 47–57 (2007).
- Ferrari, A. C. & Robertson, J. Interpretation of Raman spectra of disordered and amorphous carbon. *Phys. Rev. B* **61**, 14095–14107 (2000).
- Ferrari, A. C. & Robertson, J. Resonant Raman spectroscopy of disordered, amorphous, and diamondlike carbon. *Phys. Rev. B* **64**, 075414 (2001).
- Casiraghi, C. *et al.* Rayleigh imaging of graphene and graphene layers. *Nano Lett.* **7**, 2711–2717 (2007).
- Blake, P. *et al.* Making graphene visible. *Appl. Phys. Lett.* **91**, 063124 (2007).
- Kalbac, M. *et al.* The influence of strong electron and hole doping on the Raman intensity of chemical vapor-deposition graphene. *ACS Nano* **10**, 6055–6063 (2010).
- Chen, C. F. *et al.* Controlling inelastic light scattering quantum pathways in graphene. *Nature* **471**, 617–620 (2011).
- Casiraghi, C. *et al.* Raman fingerprint of charged impurities in graphene. *Appl. Phys. Lett.* **91**, 233108 (2007).
- Das, A. *et al.* Monitoring dopants by Raman scattering in an electrochemically top-gated graphene transistor. *Nature Nanotech.* **3**, 210–215 (2008).
- Zhao, W. J., Tan, P. H., Liu, J. & Ferrari, A. C. Intercalation of few-layer graphite flakes with FeCl₃: Raman determination of Fermi level, layer by layer decoupling, and stability. *J. Am. Chem. Soc.* **133**, 5941–5946 (2011).
- Das, A. *et al.* Phonon renormalisation in doped bilayer graphene. *Phys. Rev. B* **79**, 155417 (2009).
- Pisana, S. *et al.* Breakdown of the adiabatic Born-Oppenheimer approximation in graphene. *Nature Mater.* **6**, 198–201 (2007).
- Yan, J. *et al.* Electric field effect tuning of electron-phonon coupling in graphene. *Phys. Rev. Lett.* **98**, 166802 (2007).
- Yan, J. *et al.* Observation of anomalous phonon softening in bilayer graphene. *Phys. Rev. Lett.* **101**, 136804 (2008).
- Basko, D. M. Boundary problems for Dirac electrons and edge-assisted Raman scattering in graphene. *Phys. Rev. B* **79**, 205428 (2009).
- You, Y., Ni, Z., Yu, T. & Shen, Z. Edge chirality determination of graphene by Raman spectroscopy. *Appl. Phys. Lett.* **93**, 163112 (2008).
- Gupta, A. K., Russin, T. J., Gutiérrez, H. R. & Eklund, P. C. Probing graphene edges via Raman scattering. *ACS Nano* **3**, 45–52 (2009).
- Casiraghi, C. *et al.* Raman spectroscopy of graphene edges. *Nano Lett.* **9**, 1433–1441 (2009).
- Cong, C., Yu, T. & Wang, H. Raman study on the G mode of graphene for determination of edge orientation. *ACS Nano* **4**, 3175–3180 (2010).
- Ryu, S., Maultzsch, J., Han, M. Y., Kim, P. & Brus, L. E., Raman spectroscopy of lithographically patterned graphene nanoribbons. *ACS Nano* **5**, 4123–4130 (2011).
- Huang, M., Hugen, Y., Heinz, T. F. & Hone, J. Probing strain induced electronic structure change in graphene by Raman spectroscopy. *Nano Lett.* **10**, 4074–4079 (2010).
- Mohr, M., Maultzsch, J. & Thomsen, C. Splitting of the Raman 2D band of graphene subjected to strain. *Phys. Rev. B* **82**, 201409(R) (2010).
- Yoon, D., Son, Y. W. & Cheong, H. Strain-dependent splitting of double resonance Raman scattering band in graphene. *Phys. Rev. Lett.* **106**, 155502 (2011).
- Mohiuddin, T. M. G. *et al.* Uniaxial strain in graphene by Raman spectroscopy: G peak splitting, Gruneisen parameters, and sample orientation. *Phys. Rev. B* **79**, 205433 (2009).
- Ni, Z. H. *et al.* Uniaxial strain on graphene: Raman spectroscopy study and band-gap opening. *ACS Nano* **2**, 2301–2305 (2008).
- Proctor, J. E. *et al.* Graphene under hydrostatic pressure. *Phys. Rev. B* **80**, 073408 (2009).
- Huang, M. *et al.* Phonon softening and crystallographic orientation of strained graphene studied by Raman spectroscopy. *Proc. Natl Acad. Sci. USA* **106**, 7304–7308 (2009).
- Venezuela, P., Lazzeri, M. & Mauri, F. Theory of double-resonant Raman spectra in graphene: Intensity and line shape of defect-induced and two-phonon bands. *Phys. Rev. B* **84**, 035433 (2011).
- Lucchese, M. M. *et al.* Quantifying ion-induced defects and Raman relaxation length in graphene. *Carbon* **48**, 1592–1597 (2010).
- Cañado, L. G. *et al.* Quantifying defects in graphene via Raman spectroscopy at different excitation energies. *Nano Lett.* **11**, 3190–3196 (2011).
- Gokus, T. *et al.* Making graphene luminescent by oxygen plasma treatment. *ACS Nano* **3**, 3963–3968 (2009).
- Elias, D. C. *et al.* Control of graphene's properties by reversible hydrogenation: Evidence for graphane. *Science* **323**, 610–613 (2009).
- Nair, R. R. *et al.* Fluorographene: mechanically strong and thermally stable two-dimensional wide-gap semiconductor. *Small* **6**, 2877–2884 (2010).
- Ni, Z. *et al.* On resonant scatterers as a factor limiting carrier mobility in graphene. *Nano Lett.* **10**, 3868–3872 (2010).
- Chen, J. H., Cullen, W. G., Jang, C., Fuhrer, M. S. & Williams, E. D. Defect scattering in graphene. *Phys. Rev. Lett.* **102**, 236805 (2008).
- Balandin, A. A. *et al.* Superior thermal conductivity of single-layer graphene. *Nano Lett.* **8**, 902–907 (2008).
- Bonini, N., Lazzeri, N., Marzari, N. & Mauri, F. Phonon anharmonicities in graphite and graphene. *Phys. Rev. Lett.* **99**, 176802 (2007).
- Basko, D. M. & Aleiner, I. L. Interplay of Coulomb and electron-phonon interactions in graphene. *Phys. Rev. B* **77**, 041409(R) (2008).
- Basko, D. M. Calculation of the Raman G peak intensity in monolayer graphene: role of Ward identities. *New J. Phys.* **11**, 095011 (2009).
- Basko, D. M. Theory of resonant multiphonon Raman scattering in graphene. *Phys. Rev. B* **78**, 125418 (2008).
- Grüneis, A. *et al.* Phonon surface mapping of graphite: Disentangling quasi-degenerate phonon dispersions. *Phys. Rev. B* **80**, 085423 (2009).
- May, P. *et al.* Signature of the two-dimensional phonon dispersion in graphene probed by double-resonant Raman scattering. *Phys. Rev. B* **87**, 075402 (2013).
- Lazzeri, M. *et al.* Impact of the electron-electron correlation on phonon dispersion: Failure of LDA and GGA DFT functionals in graphene and graphite. *Phys. Rev. B* **78**, 081406(R) (2008).
- Lazzeri, M. & Mauri, F. Nonadiabatic Kohn anomaly in a doped graphene monolayer. *Phys. Rev. Lett.* **97**, 266407 (2006).
- Faugeras, C. *et al.* Tuning the electron-phonon coupling in multilayer graphene with magnetic fields. *Phys. Rev. Lett.* **103**, 186803 (2009).
- Kossacki, P. *et al.* Electronic excitations and electron-phonon coupling in bulk graphite through Raman scattering in high magnetic fields. *Phys. Rev. B* **84**, 235138, (2011).
- Faugeras, C. *et al.* Magneto-Raman scattering of graphene on graphite: Electronic excitations and their coupling to optical phonons. *Phys. Rev. Lett.* **107**, 036807 (2011).
- Kim, Y. *et al.* Magnetophonon resonance in graphite: High-field Raman measurements and electron-phonon coupling contributions. *Phys. Rev. B* **121403(R)** (2012).
- Kim, Y. *et al.* Filling-factor-dependent magnetophonon resonance with circularly polarized phonons in graphene revealed by high-field magneto-Raman spectroscopy. Preprint at <http://arxiv.org/abs/1211.6094> (2012).
- Faugeras, C. *et al.* Effect of a magnetic field on the two-phonon Raman scattering in graphene. *Phys. Rev. B* **81**, 155436 (2010).
- Faugeras, C. *et al.* Probing the band structure of quadri-layer graphene with magneto-phonon resonance. *New J. Phys.* **14**, 095007 (2012).
- Yan, J. *et al.* Observation of magneto-phonon resonance of Dirac fermions in graphite. *Phys. Rev. Lett.* **105**, 227401 (2010).
- Goerbig, M. O. *et al.* Filling-factor-dependent magnetophonon resonance in graphene. *Phys. Rev. Lett.* **99**, 087402 (2007).
- Ando, T. Magnetic oscillation of optical phonon in graphene. *J. Phys. Soc. Jpn* **76**, 024712 (2007).

68. Tan, P. H. *et al.* The shear mode of multilayer graphene. *Nature Mater.* **11**, 294–300 (2012).
69. Lui, C. *et al.* Observation of layer-breathing mode vibrations in few-layer graphene through combination Raman scattering. *Nano Lett.* **12**, 5539–5544 (2012).
70. Lui, C. H. & Heinz, T. F. Measurement of layer breathing mode vibrations in few-layer graphene. *Phys. Rev. B* **87**, 121404 (2013).
71. Sato, K. *et al.* Raman spectra of out-of-plane phonons in bilayer graphene. *Phys. Rev. B* **84**, 035419 (2011).
72. Herziger, F., May, F. & Maultzsch, J. Layer number determination in graphene using out-of-plane vibrations. *Phys. Rev. B* **85**, 235447 (2012).
73. Maultzsch, J., Reich, S. & Thomsen, C. Double-resonant Raman scattering in graphite: Interference effects, selection rules, and phonon dispersion. *Phys. Rev. B* **70**, 155403 (2004).
74. Yoon, D. *et al.* Interference effect on Raman spectrum of graphene on SiO₂/Si. *Phys. Rev. B* **80**, 125422 (2009).
75. Wang, Y. Y. *et al.* Interference enhancement of Raman signal of graphene. *Appl. Phys. Lett.* **92**, 043121 (2008).
76. Schedin, F. *et al.* Surface enhanced Raman spectroscopy of graphene. *ACS Nano* **4**, 5617–5626 (2010).
77. Malard, L. M., Pimenta, M. A., Dresselhaus, G. & Dresselhaus, M. S. Raman spectroscopy in graphene. *Phys. Rep.* **473**, 51–87 (2009).
78. Jorio, A., Dresselhaus, M. S., Saito, R. & Dresselhaus, G. *Raman Spectroscopy in Graphene Related Systems* (Wiley, 2011).
79. Saito, R., Hofmann, M., Dresselhaus, G., Jorio, A. & Dresselhaus, M. S. Raman spectroscopy of graphene and carbon nanotubes. *Adv. Phys.* **60**, 413–550 (2011).
80. Piscanec, S., Lazzeri, M., Mauri, F., Ferrari, A. C. & Robertson, J. Kohn anomalies and electron-phonon interactions in graphite. *Phys. Rev. Lett.* **93**, 185503 (2004).
81. Nemanich, R. J., Lucovsky, G. & Solin, S. A. Infrared active optical vibrations of graphite. *Solid State Comm.* **23**, 117–120 (1977).
82. Reich, S. & Thomsen, C. Raman spectroscopy of graphite. *Phil. Trans. R. Soc. A* **362**, 2271–2288 (2004).
83. Mani, K. K. & Ramani, R. Lattice dynamics of graphite. *Phys. Stat. Sol. B* **61**, 659–668 (1974).
84. Maultzsch, J., Reich, S., Thomsen, C., Requardt, H. & Ordejón, P. Phonon dispersion in graphite. *Phys. Rev. Lett.* **92**, 075501 (2004).
85. Thomsen, C. & Reich, S. Double resonant Raman scattering in graphite. *Phys. Rev. Lett.* **85**, 5214–5217 (2000).
86. Baranov, A. V. *et al.* Interpretation of certain characteristics in Raman spectra of graphite and glassy carbon. *Opt. Spectroscopy* **62**, 612–616 (1987).
87. Pocsik, I., Hundhausen, M., Koos, M. & Ley, L. Origin of the D peak in the Raman spectrum of microcrystalline graphite. *J. Non-Cryst. Solids* **227–230**, 1083–1086 (1998).
88. Basko, D. M., Piscanec, S. & Ferrari, A. C. Electron-electron interactions and doping dependence of the two-phonon Raman intensity in graphene. *Phys. Rev. B* **80**, 165413 (2009).
89. Nemanich, R. J. & Solin, S. A. First- and second-order Raman scattering from finite-size crystals of graphite. *Phys. Rev. B* **20**, 392–401 (1979).
90. Tan, P. H., Deng, Y. M. & Zhao, Q. Temperature-dependent Raman spectra and anomalous Raman phenomenon of highly oriented pyrolytic graphite. *Phys. Rev. B* **58**, 5435–5439 (1998).
91. Tan, P. H. *et al.* Probing the phonon dispersions of graphite from the double-resonance process of Stokes and anti-Stokes Raman scatterings in multiwalled carbon nanotubes. *Phys. Rev. B* **66**, 245410 (2002).
92. Tan, P. H., Hu, C. Y., Dong, J., Shen, W. C. & Zhang, B. F. Polarization properties, high-order Raman spectra, and frequency asymmetry between Stokes and anti-Stokes scattering of Raman modes in a graphite whisker. *Phys. Rev. B* **64**, 214301 (2001).
93. Kawashima, Y. & Katagiri, G. Fundamentals, overtones, and combinations in the Raman spectrum of graphite. *Phys. Rev. B* **52**, 10053–10059 (1995).
94. Nemanich, R. J., Lucovsky, G. & Solin, S. A. in *Proc. Int. Conf. on Lattice Dynamics* (ed. Balkanski, M.) 619–621 (Flammarion, 1975).
95. Zhang, X. *et al.* Raman spectroscopy of shear and layer breathing modes in Multilayer MoS₂. *Phys. Rev. B* **87**, 115413 (2013).
96. Latil, S., Meunier, V. & Henrard, L. Massless fermions in multilayer raphitic systems with misoriented layers: *Ab initio* calculations and experimental fingerprints. *Phys. Rev. B* **76**, 201402(R) (2007).
97. Wallace, P. R. The band theory of graphite. *Phys. Rev.* **71**, 622–634 (1948).
98. Kashuba, A. & Fal'ko, V. I. Signature of electronic excitations in the Raman spectrum of graphene. *Phys. Rev. B* **80**, 241404 (2009).
99. Kashuba, O. & Fal'ko, V. I., Role of electronic excitations in magneto-Raman spectra of graphene. *New J. Phys.* **14**, 105016 (2012).
100. Wang, F. *et al.* Multiphonon Raman scattering from individual single-walled carbon nanotubes. *Phys. Rev. Lett.* **98**, 047402 (2007).
101. Rao, R., Tishler, D., Katoch, J. & Ishigami, M. Multiphonon Raman scattering in graphene. *Phys. Rev. B* **84**, 113406 (2011).
102. Yu, P. Y. & Cardona, M. *Fundamentals of Semiconductors* (Springer, 2005).
103. Zeyher, R. Calculation of resonant second-order Raman efficiencies for allowed and forbidden scattering. *Phys. Rev. B* **9**, 4439–4447 (1974).
104. Goltsev, A. V., Lang, I. G., Pavlov, S. T. & Bryzhina, M. F. Multiphonon resonance Raman scattering and spatial distribution of electrons and holes. *J. Phys. C* **16**, 4221–4241 (1983).
105. Martin, R. M. Resonance Raman scattering near critical points. *Phys. Rev. B* **10**, 2620–2631 (1974).
106. Vidano, R. P., Fishbach, D. B., Willis, L. J. & Loehr, T. M. *Solid State Commun.* **39**, 341–344 (1981).
107. Mafrá, D. L. *et al.* Determination of LA and TO phonon dispersion relations of graphene near the Dirac point by double resonance Raman scattering. *Phys. Rev. B* **76**, 233407 (2007).
108. Basko, D. M. Effect of anisotropic band curvature on carrier multiplication in graphene. Preprint at <http://arXiv.org/abs/1302.5891> (2013).
109. Golub, L. E., Tarasenko, S. A., Entin, M. V. & Magarill, L. I. Valley separation in graphene by polarized light. *Phys. Rev. B* **84**, 195408 (2011).
110. Mafrá, D. L., Moujaes, E. A., Nunes, R. W. & Pimenta, M. A. On the inner double-resonance Raman scattering process in bilayer graphene. *Carbon* **49**, 1511–1515 (2011).
111. Cañado, L. G. *et al.* Stokes and anti-Stokes double resonance Raman scattering in two-dimensional graphite. *Phys. Rev. B* **66**, 035415 (2002).
112. Cañado, L. G., Jorio, A. & Pimenta, M. A. Measuring the absolute Raman cross section of nanographites as a function of laser energy and crystallite size. *Phys. Rev. B* **76**, 064304 (2007).
113. Yang, L., Deslippe, J., Park, C.-H., Cohen, M. L. & Louie, S. G. Excitonic effects on the optical response of graphene and bilayer graphene. *Phys. Rev. Lett.* **103**, 186802 (2009).
114. Kravets, V. G. *et al.* Spectroscopic ellipsometry of graphene and an exciton-shifted van Hove peak in absorption. *Phys. Rev. B* **81**, 155413 (2010).
115. Cervantes-Sodi, F., Csányi, G., Piscanec, S. & Ferrari, A. C. Edge functionalized and substitutionally doped graphene nanoribbons: Electronic and spin properties. *Phys. Rev. B* **77**, 165427 (2008).
116. Nemes-Incze, P., Magda, G., Kamars, K. & Bir, L. P. Crystallographically selective nanopatterning of graphene on SiO₂. *Nano Res.* **3**, 110–116 (2010).
117. Girit, Ç. O. *et al.* Graphene at the edge: Stability and dynamics. *Science* **323**, 1705–1708 (2009).
118. Kobayashi, K., Fukui, K., Enoki, T., Kusakabe, K. & Kaburagi, Y. Observation of zigzag and armchair edges of graphite using scanning tunneling microscopy and spectroscopy. *Phys. Rev. B* **71**, 193406 (2005).
119. Cañado, L. G. *et al.* Influence of the atomic structure on the Raman spectra of graphite edges. *Phys. Rev. Lett.* **93**, 247401 (2004).
120. Sasaki, K. *et al.* Kohn anomalies in graphene nanoribbons. *Phys. Rev. B* **80**, 155450 (2009).
121. Begliarbekov, M., Sasaki, K.-I., Sul, O., Yang, E.-H. & Strauf, S. Optical control of edge chirality in graphene. *Nano Lett.* **11**, 4874–4878 (2011).
122. Malard, L. M. *et al.* Probing the electronic structure of bilayer graphene by Raman scattering. *Phys. Rev. B* **76**, 201401(R) (2007).
123. Cañado, L. G. *et al.* Geometrical approach for the study of G' band in the Raman spectrum of monolayer graphene, bilayer graphene, and bulk graphite. *Phys. Rev. B* **77**, 245408 (2008).
124. Lukyanchuk, I. A., Kopelevich, Y. & El Marssi, M. Dirac fermions in graphite: The state of art. *Physica B* **404**, 404–406 (2009).
125. Lespade, P. *et al.* Characterisation de matériaux carbonés par microspectrométrie Raman. *Carbon* **22**, 375–385 (1984).
126. Lui, C. H. *et al.* Imaging stacking order in few-layer graphene. *Nano Lett.* **11**, 164–169 (2011).
127. Kim, K. *et al.* Raman spectroscopy study of rotated double-layer graphene: Misorientation-angle dependence of electronic structure. *Phys. Rev. Lett.* **108**, 246103 (2012).
128. Gupta, A. K., Tang, T., Crespi, V. H. & Eklund, P. C. Nondispersive Raman D band activated by well-ordered interlayer interactions in rotationally stacked bilayer graphene. *Phys. Rev. B* **82**, 241406(R) (2010).
129. Carozo, V. *et al.* Raman signature of graphene superlattices. *Nano Lett.* **11**, 4527–4534 (2011).
130. Jorio, A. *et al.* Linewidth of the Raman features of individual single-wall carbon nanotubes. *Phys. Rev. B* **66**, 115411 (2002).
131. Pfeiffer, R. *et al.* Resonance Raman scattering from phonon overtones in double-wall carbon nanotubes. *Phys. Rev. B* **71**, 155409 (2005).
132. Dean, C. R. *et al.* Boron nitride substrates for high-quality graphene electronics. *Nature Nanotech.* **5**, 722–726 (2010).
133. Matthews, M. J., Pimenta, M. A., Dresselhaus, G., Dresselhaus, M. S. & Endo, M. Origin of dispersive effects of the Raman D band in carbon materials. *Phys. Rev. B* **59**, R6585–R6588 (1999).

134. Knight, D. S. & White, W. B. Characterization of diamond films by Raman spectroscopy. *J. Mater. Res.* **4**, 385–393 (1989).
135. Beams, R., Cançado, L. G. & Novotny, L. Low temperature Raman study of the electron coherence length near graphene edges. *Nano Lett.* **11**, 1177–1181 (2011).
136. Ferrari, A. C. *et al.* Interpretation of infrared and Raman spectra of amorphous carbon nitrides. *Phys. Rev. B* **67**, 155306 (2003).
137. Novoselov, K. S. *et al.* Two-dimensional atomic crystals. *Proc. Natl Acad. Soc. USA* **102**, 10451–10453 (2005).
138. Nemanich, R. J., Solin, S. A. & Martin, R. M. Light-scattering study of boron-nitride microcrystals. *Phys. Rev. B* **23**, 6348–6356 (1981).
139. Arenal, R. *et al.* Raman spectroscopy of single-wall boron nitride nanotubes. *Nano Lett.* **6**, 1812–1816 (2006).
140. Reich, S. *et al.* Resonant Raman scattering in cubic and hexagonal boron nitride. *Phys. Rev. B* **71**, 205201 (2005).
141. Russo, V. *et al.* Raman spectroscopy of Bi-Te thin films. *J. Raman Spectrosc.* **39**, 205–210 (2008).
142. Verble, J. L. & Wieting, T. J. Lattice mode degeneracy in MoS₂ and other layer compounds. *Phys. Rev. Lett.* **25**, 362–365 (1970).
143. Lee, C., Yan, H., Brus, L. E., Heinz, T. F., Hone, J. & Ryu, S. Anomalous lattice vibrations of single- and few-layer MoS₂. *ACS Nano* **4**, 2695–2700 (2010).
144. Novoselov, K. S. & Castro Neto, A. H. Two-dimensional crystals-based heterostructures: materials with tailored properties. *Phys. Scr.* **T146**, 014006 (2012).

Acknowledgements

We thank E. Lidorikis, S. Piscanec, P. H. Tan, S. Milana, D. Yoon, A. Lombardo, A. Bonetti, C. Casiraghi, F. Bonaccorso, G. Savini, N. Bonini, N. Marzari, T. Kulmala, A. Jorio, M. A. Pimenta, G. Cancado, R. Ruoff, R. A. Nair, K. A. Novoselov, L. Novotny, A. K. Geim, C. Faugeras and M. Potemski for useful discussions. A.C.F. acknowledges funding from the Royal Society, the European Research Council Grant NANOPOTS, EU grants RODIN, GENIUS, MEM4WIN and CareRAMM, EPSRC grants EP/K01711X/1, EP/K017144/1, EP/G042357/1, and Nokia Research Centre, Cambridge.

Additional information

Supplementary information is available in the online version of the paper. Reprints and permissions information is available online at www.nature.com/reprints. Correspondence should be addressed to A.C.F.

Competing financial interests

The authors declare no competing financial interests.